Article

Deconvoluting Kinetic Rate Constants of Catalytic Substrates from Scanning Electrochemical Approach Curves with Artificial Neural Networks

Dinuka Rajapakse, Josh Meckstroth, Dylan T. Jantz, Kyle Vincent Camarda, Zijun Yao, and Kevin C. Leonard*

Cite This: *ACS Meas. Sci. Au* 2023, 3, 103–112

Read Online

| ACCESS | 📊 Metrics & More | 📖 Article Recommendations | 🔵 Supporting Information |

ABSTRACT: Extracting information from experimental measurements in the chemical sciences typically requires curve fitting, deconvolution, and/or solving the governing partial differential equations via numerical (e.g., finite element analysis) or analytical methods. However, using numerical or analytical methods for high-throughput data analysis typically requires significant postprocessing efforts. Here, we show that deep learning artificial neural networks can be a very effective tool for extracting information from experimental data. As an example, reactivity and topography information from scanning electrochemical microscopy (SECM) approach curves are highly convoluted. This study utilized multilayer perceptrons and convolutional neural networks trained on simulated SECM data to extract kinetic rate constants of catalytic substrates. Our key findings were that multilayer perceptron models performed very well when the experimental data were close to the ideal conditions with which the model was trained. However, convolutional neural networks, which analyze images as opposed to direct data, were able to accurately predict the kinetic rate constant of Fe-doped nickel (oxy)hydroxide catalyst at different applied potentials even though the experimental approach curves were not ideal. Due to the speed at which machine learning models can analyze data, we believe this study shows that artificial neural networks could become powerful tools in high-throughput data analysis.

KEYWORDS: *scanning electrochemical microscopy, machine learning, artificial neural networks, convolutional neural networks, data analysis*
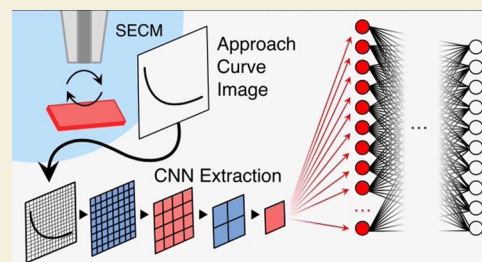
1. INTRODUCTION

Scanning electrochemical microscopy (SECM) is a scanning probe technique that can obtain spatial-dependent surface reactivity and topography of solid surfaces operating in a solution phase.[1−8] In SECM, the probe is typically a micro- or nanoelectrode (referred to as a tip electrode), and reactivity and topography of the surface (referred to as the substrate) are determined via detecting the flux of redox-active molecules between the tip and substrate through current measurements on the tip electrode.[8−10] Spatial-dependent information is typically obtained by raster-scanning the tip electrode in the $x-y$ plane over the substrate of interest.[11−16] However, a challenge in SECM is that the reactivity and topography are often convoluted because the flux of the redox mediators is dependent on both the reactivity of the substrate and the tip/substrate distance.[17] Thus, it is common practice to perform an additional *ex situ* imaging technique in parallel with SECM to obtain separate topography information so reactivity information can be inferred.[18]

Recently, the Amemiya and Leonard groups have developed an intelligent mode of nanoscale SECM to image both reactivity and topography simultaneously of nonflat substrates with reactive and inert regions.[19,20] This intelligent imaging mode is based on the analysis of approach curves taken at different positions over the substrate of interest. The power of this approach curve mapping technique is that it can unequivocally determine the reactivity and the topography because the tip is approached toward the substrate at each pixel in the image. However, the challenge with intelligent SECM is converting the direct current measurement to topography and reactivity in real time. This deconvolution requires solving complex partial differential equations (e.g., Fick's diffusion with potential-dependent flux boundary conditions) in three-dimensional space via finite element analysis software and/or postmeasurement fitting of experimental data to nonlinear analytical models.[2] This data analysis

adds significant postprocessing time and limits the total number of pixels that can be obtained in an image.

Here, we report on using machine learning techniques as an alternative to finite elemental analysis and nonlinear curve fitting for obtaining the substrate kinetics of SECM approach curves. Simply put, machine learning models use mathematical algorithms to uncover patterns within the data provided to the system.[21] Bond, Compton, Liu, and others have used machine learning and artificial neural networks to analyze electrochemical cyclic voltammetry data, mainly via classification algorithms to predict mechanisms.[22−26] Similar to voltammetry, the observed shape of an SECM approach curve is dependent on the kinetic rate constant of the substrate reaction. Our goal was to determine if machine learning algorithms could calculate the kinetic rate constant of a substrate without actually solving the partial differential equations that govern the process. Specifically, we investigated the use of two types of artificial neural network machine learning algorithms, multilayer perceptrons (MLP) and convolutional neural networks (CNN). MLP models pass an entire data set through multiple layers of nodes (i.e., perceptrons) where each node acts analogous to a transfer function where inputs are multiplied by weights and entered into an activation function to obtain an output. Training the model to convert the input data set into an output is done through back-propagation where the weights of the neural network are tuned based on the error of the previous iteration (i.e., epoch).[27−30] CNN models are typically used for image classification, for example, they are used to detect letters and numbers in handwriting analysis.[31−43] In general, a CNN makes a classification via scanning through the image to extract features in a hierarchical manner, starting with the low-level features and then utilizing the final feature map in an MLP for the final classification.

All machine learning models need large amounts of data for training. Here, we used data generated from analytical expressions previously derived to capture how the shape of SECM approach curves changes as a function of the kinetic rate constant of the substrate.[2] We investigated two different methods of utilizing SECM approach curve data with MLP models—(1) only the measured current data and (2) the slope of the current vs z-position data. Since CNN models are typically trained on image data, the approach curves were converted to image form for use in the CNN model. Validation of the model was performed by performing experimental approach curves on a Fe-doped nickel (oxy)hydroxide substrate. While this material has practical significance as an electrocatalyst for the oxygen evolution reaction (OER),[44−46] this material was chosen because it has the unique property of transitioning from completely insulating to completely conducting as a function of potential. Thus, on the same substrate, we can obtain electron-transfer kinetic rate constants on an outer-sphere redox process spanning several orders of magnitude.

We observed that both the MLP and CNN models can obtain very high accuracy on ideal SECM approach curves. However, on nonideal SECM approach curves, where the nonideality occurs from a combination of rough surfaces with tip/substrate misalignment, the CNN model outperforms the MLP models. We attribute this to the CNN model being able to obtain the general trend via analyzing the image as opposed to the raw data. We envision this machine learning technique will not only impact the rapid analysis of SECM approach curves but could be applied to other areas of data analysis where numerous experiments need to be quantified.

2. EXPERIMENTAL AND COMPUTATIONAL METHODS

2.1. Computational Methods

2.1.1. Data Set and Data Processing. Two separate data sets were synthesized: one for the multilayer perceptron (MLP) and the other for the convolutional neural network (CNN). The data for the MLP consisted of 2250 approach curves, the current values of which were calculated using the expression derived by Lefrou et al.[2]

$$\frac{i_T^{NF}(L)}{i_{T,\infty}} =$$

$$\frac{\frac{2.08}{R_g^{0.358}}\left(L - \frac{0.145}{R_g}\right) + 1.585}{\frac{2.08}{R_g^{0.358}}(L + 0.0023R_g) + 1.57 + \frac{\ln R_g}{L} + \frac{2}{\pi R_g}\ln\left(1 + \frac{\pi R_g}{2L}\right)} \quad (1)$$

$$\frac{i_T^{PF}(L)}{i_{T,\infty}} = \alpha + \frac{\pi}{4\beta \arctan(L)} + \left(1 - \alpha - \frac{1}{2\beta}\right)\frac{2}{\pi}\arctan(L) \quad (2)$$

$$\frac{i_T(L, \kappa)}{i_{T,\infty}} = \frac{i^{PF}\left(L + \frac{1}{\kappa}\right)}{i_{T,\infty}}$$

$$+ \frac{\frac{i_T^{NF}(L)}{i_{T,\infty}} - 1}{(1 + 2.47R_g^{0.31}L\kappa)(1 + L^{0.006R_g + 0.113}\kappa^{-0.0236R_g + 0.91})} \quad (3)$$

where R_g is the ratio of the radius of the insulation sheath around the electrode to the radius of the disk electrode (r_{glass}/a); L is the ratio of the distance the tip is away from the substrate to the radius of the disk electrode (d/a); and κ, α, and β are described as follows

$$\kappa = \frac{ka}{D} \quad (4)$$

$$\alpha = \ln 2 + \ln 2\left(1 - \frac{2}{\pi}\arccos\left(\frac{1}{R_g}\right)\right)$$
$$- \ln 2\left(1 - \left(\frac{2}{\pi}\arccos\left(\frac{1}{R_g}\right)\right)^2\right) \quad (5)$$

$$\beta = 1 + 0.639\left(1 - \frac{2}{\pi}\arccos\left(\frac{1}{R_g}\right)\right) - 0.186$$
$$\left(1 - \left(\frac{2}{\pi}\arccos\left(\frac{1}{R_g}\right)\right)^2\right) \quad (6)$$

where k is the kinetic rate constant of the substrate, D is the diffusion coefficient of the redox mediator, and a is the radius of the tip electrode.

Each approach curve in the model was unique, each having a different substrate rate constant value and a final tip−substrate distance. The rate constant values range from 1 to 10^{-5} cm s^{-1} with a diffusion coefficient of 10^{-5} cm^2 s^{-1}. The final tip−substrate distances ranged d/a values (where d is the tip−substrate distance and a is the radius of the electrode) from 0.1 to 2. Each approach curve consisted of 150 points.

The data for the CNN consisted of 3800 images of approach curves. These images were 100 pixel by 100 pixel grayscale images
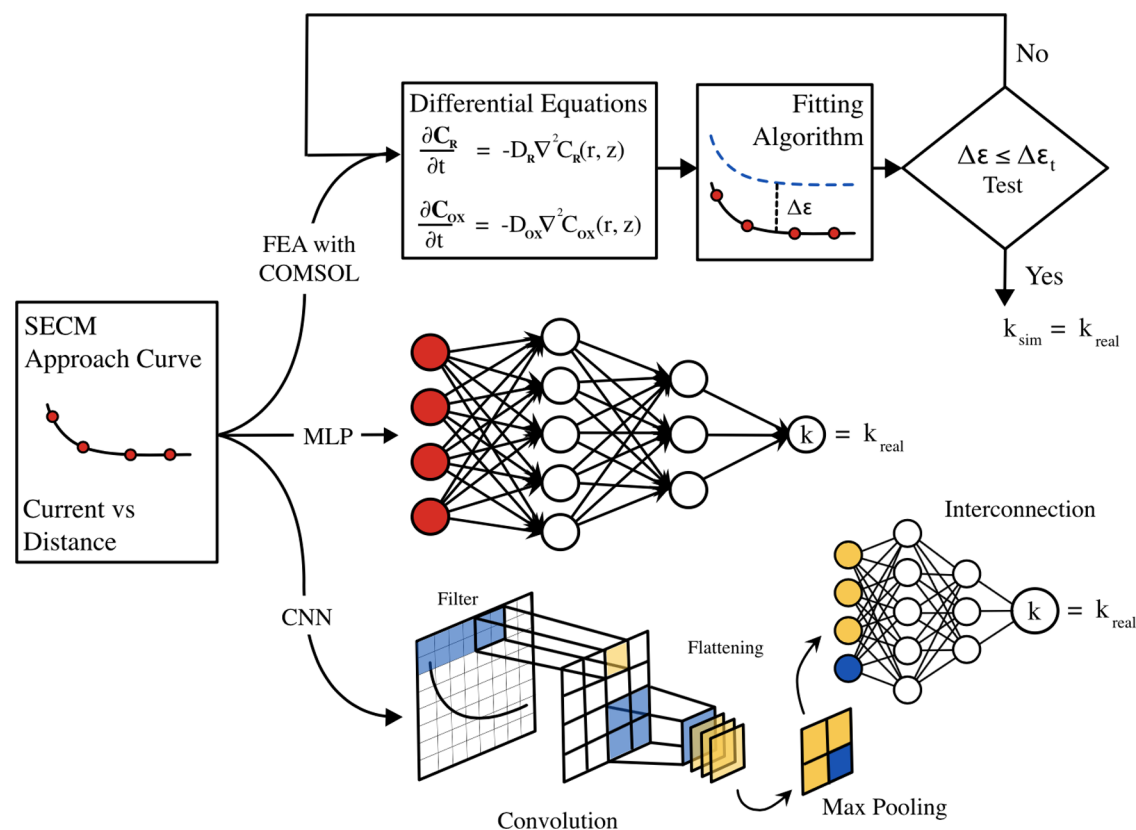
Figure 1. Overview of three different methods of obtaining a substrate kinetic rate constant from SECM approach curves. Using finite elemental analysis or analytical expressions to solve diffusion equations, which govern how the tip current changes with substrate kinetics (top). Entering raw approach curve data into a multilayer perceptron model to obtain the kinetic rate constant (middle) and using the image of an approach curve in a convolutional neural network to obtain a kinetic rate constant (bottom).

that did not include the x and y axes or axis labels. Each of these approach curves also has a unique rate constant value and a final tip–substrate distance. The rate constant values ranged from 1 to 10^{-3} cm s^{-1}, the diffusion coefficient was 10^{-5} cm^2 s^{-1}, and the final tip–substrate distance values ranged from d/a values of 0.01 to 0.3.

2.1.2. Machine Learning Packages. All machine learning algorithms were programmed in Python using Jupyter Notebooks. The Keras library, a wrapper for the Tensorflow, was used as the machine learning library to implement both the MLP and CNN algorithms. All source code for this study can be found in the Supporting Information. Two MLP models were built: MLP-C and MLP-S. Both models only used the ReLu activation function in all hidden layers. The MLP-C model consisted of three hidden layers each having 10 nodes. The MLP-S model consisted of four hidden layers, where the first three layers consisted of 10 nodes each and the last hidden layer consisted of five nodes. The MLP regression models were trained over 1000 epochs. The CNN model consisted of two feature extractors, each of which consisted of a convolutional layer followed by a max pooling layer. The dimension of all max pooling layers was 2 × 2. The first convolutional layer used a 10 × 10 kernel to output a 32 × 32 lower-level feature map. The second convolutional layer used a 5 × 5 kernel, which outputs a 10 × 10 higher-level feature map. Both feature extractors use ReLu as the activation function all throughout and a dropout of 0.25. The first and only hidden layer of the MLP attached to the second extractor consisted of 256 nodes and uses the ReLu activation function as well. The final output layer consisted of 10 nodes to represent the 10 classes, and it uses the softmax activation function.

2.1.3. Model Evaluation. Both data sets were split into training and testing sets, with an 80:20 split. Mean-squared error and mean absolute error were used to determine the quality of the regression MLP model. Accuracy, precision, recall, and F-1 score were used to evaluate the multiclass classification CNN model.

2.2. Experimental Methods

2.2.1. Chemicals and Materials. Iron(III) nitrate nonahydrate ($Fe(NO_3)_3 \cdot 9H_2O$, 98%+, ACS Reagent, Acros), nickel nitrate hexahydrate ($Ni(NO_3)_2 \cdot 6H_2O$, 99%, Fisher Scientific), ethylene glycol (($CH_2OH)_2$, 99.8%, anhydrous, Sigma-Aldrich), sodium hydroxide (NaOH, 98.7%, Certified ACS, Fisher Scientific), potassium chloride (KCl, 99%+, Certified ACS, Fisher Scientific), and hexaammineruthenium(III) chloride ($Ru(NH_3)_6 Cl_3$, 99%, Strem Chemicals) were all used as received without additional purification. The electrolyte solution was prepared using ultrapure water (18.2 MΩ cm) from Millipore Synergy UV system. Platinum wire (purity 99.9%, 0.01 mm diameter, temper hard, Good Fellow) was used for tip electrode fabrication. The 10 μm Pt microelectrode was manufactured following the same procedure as previously described.[4]

2.2.2. Fe-Doped Nickel (Oxy)hydroxide Synthesis. The Fe-doped nickel (oxy)hydroxide crystalline-derived catalyst was synthesized following the same procedure as previously described.[44,45] Briefly, mixtures of 0.02 M $Ni(NO_3)_2 \cdot 6H_2O$ and 0.02 M $Fe(NO_3)_3 \cdot 9H_2O$ were prepared separately in ethylene glycol and subsequently added together in an 8:2 ratio. This solution was drop-cast on cleaned fluorine-doped tin oxide (FTO)-coated glass (Sigma-Aldrich) and placed into an oven at 135 °C for 30 min, then repeated once more for a second coating. The crystalline thin-film samples were further annealed at 525 °C for 3 h to create the Fe-doped nickel (oxy)hydroxide layer. The Fe-doped nickel (oxy)hydroxide was then electrochemically conditioned by applying an oxidation current of ca. 10 mA cm^2 in 1 M NaOH for 1 h.

2.2.3. Scanning Electrochemical Microscopy Measurements. All SECM experiments were performed via a custom-built SECM, as previously described.[47] The Fe-doped nickel (oxy)-hydroxide crystalline catalyst was inserted into a custom electrochemical cell (Teflon) as the substrate electrode, which was then

mounted on the motion controller system. A 200 μm Pt wire coil was used as the counter electrode, and an Ag/AgCl electrode was used as the reference. The electrolyte solution used was 10 mM $Ru(NH_3)_6^{3+}$, thoroughly purged with argon before use. The 10 μm Pt microelectrode was used as the SECM tip electrode for SECM experiments. The Pt tip electrode was initially placed in close proximity to the desired hole in the Fe-doped nickel (oxy)hydroxide crystalline catalyst by visual alignment.

The first series of SECM experiments were performed in the 10 mM $Ru(NH_3)_6^{3+}$ solution. A CV was performed from +0.05 to −0.3 V vs Ag/AgCl to verify the reduction potential range of $Ru(NH_3)_6^{3+}$ to $Ru(NH_3)_6^{2+}$. To bring the tip close to the catalyst surface, a reducing potential of −0.3 V vs Ag/AgCl was applied on the tip electrode as it was stepped toward the substrate until a current enhancement of 0.5 was reached. The tip electrode was then raster scanned over a 300 μm × 300 μm region while still holding −0.3 V vs Ag/AgCl to find the desired hole in the Fe-doped nickel (oxy)hydroxide crystalline catalyst. Once positioned, smaller reactivity maps (150 μm × 150 μm) with higher resolution (3 μm) and sample interval of 0.4 s were performed. For each of these maps, the tip electrode was held at −0.3 V vs Ag/AgCl, while the substrate was varied from +0.05 to +0.8 V vs Ag/AgCl. Finally, approach curves were obtained over the Fe-doped nickel (oxy)hydroxide sample at various substrate potentials to change the kinetics of the $Ru(NH_3)_6^{3+}$ to $Ru(NH_3)_6^{2+}$ reaction.

3. RESULTS AND DISCUSSION

Two different artificial neural networks, multilayer perceptron (MLP) and convolutional neural networks (CNN), were
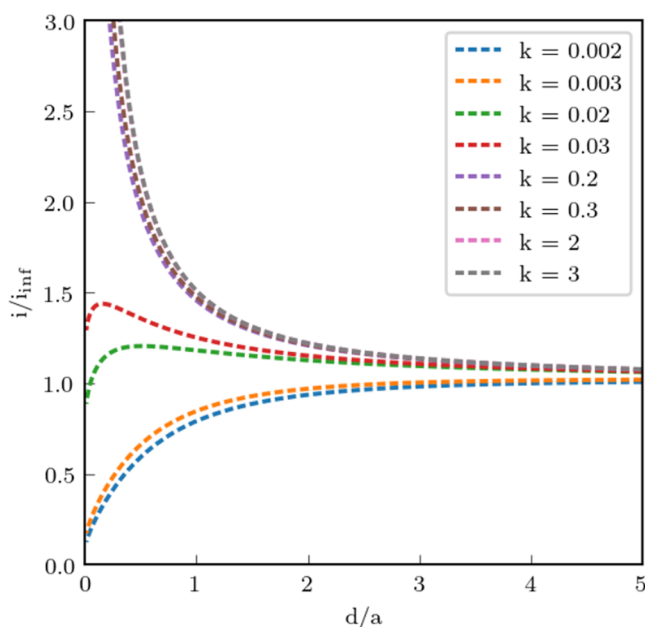
Figure 2. Example SECM approach curves showing pure positive feedback at fast substrate rate constants, pure negative feedback at slow substrate rate constants, and mixed feedback at intermediate rate constants (k = cm s^{-1}).

evaluated to determine their ability to calculate the substrate kinetic rate constants of SECM approach curves. This was compared to traditional approaches of using finite elemental analysis or analytical solutions to Fick's diffusion equations, which govern the flux of redox-active molecules between the tip and substrate of SECM experiments (Figure 1).

To train the models, SECM approach curves were simulated using eqs 1−6 as shown above.[2] As shown in Figure 2, there is a dramatic change in the shape of an SECM approach curve
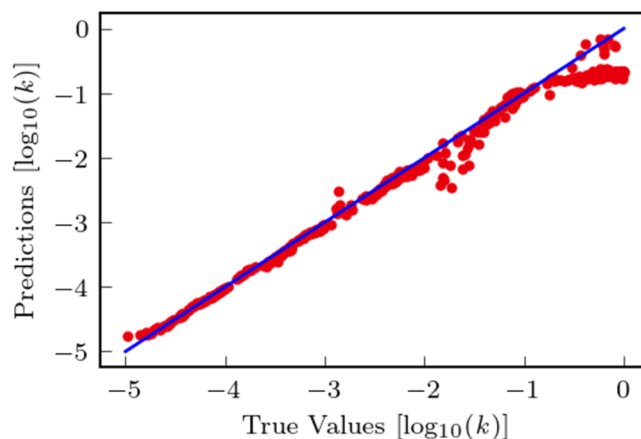
Figure 3. Comparison between the predicted substrate kinetic rate constant from the MLP-C model to the known substrate kinetic rate constant (red points). The blue 45° line is the perfect prediction comparison line.

Figure 4. Comparison between the predicted substrate kinetic rate constant from the MLP-S model to the known substrate kinetic rate constant (red points). The blue 45° line is the perfect prediction comparison line.
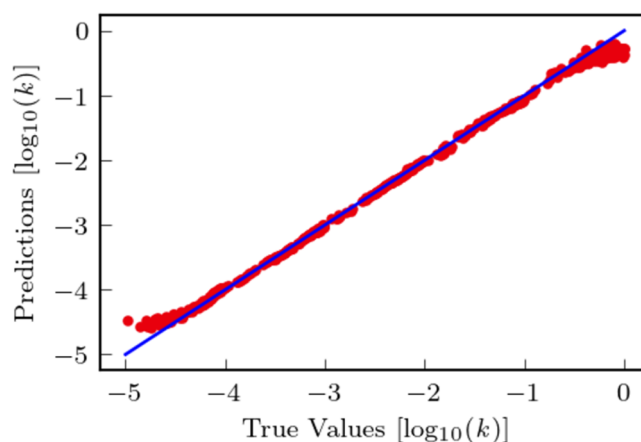
Table 1. Range of Substrate Kinetic Rate Constants for Each Class, in the Multiclass Classification CNN Model

class no.	min k(cm s^{-1})	max k(cm s^{-1})
0	0.001	0.0029
1	0.003	0.0049
2	0.005	0.0069
3	0.007	0.0089
4	0.009	0.0099
5	0.01	0.029
6	0.03	0.049
7	0.05	0.069
8	0.07	0.089
9	0.09	0.1

based on the kinetics of the substrate. For rate constants slower than 10^{-3} cm s^{-1}, the approach curve approaches pure negative feedback where the hindered diffusion caused by the close tip/substrate distance governs the flux of the redox molecules towards the tip electrode. Contrastingly, when the substrate kinetic rate constants exceed 1 cm s^{-1}, the approach curve

Table 2. Precision, Recall, and *F*-1 Score of the Training Set for the CNN Model for Each of the 10 Classes

class no.	precision	recall	F-1 score
0	1.00	0.98	0.99
1	0.98	0.98	0.98
2	0.98	0.96	0.97
3	0.95	1.00	0.97
4	0.95	0.99	0.97
5	1.00	0.93	0.96
6	0.66	0.97	0.79
7	0.51	0.20	0.29
8	0.42	0.78	0.54
9	0.76	0.23	0.35
accuracy: 0.80			
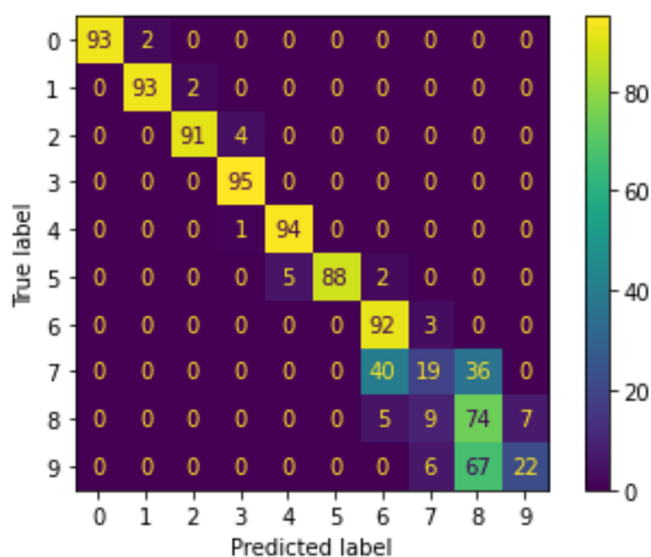
Figure 5. Confusion matrix showing the predicted result vs the actual result for each of the 16 classes for the multiclass CNN model.

becomes pure positive feedback where the increase of mass transfer of the redox-active molecule is caused by complete conversion at the substrate. For all kinetics between these values, mixed feedback is observed. Because the shape of the approach curve is different for each kinetic rate constant, we hypothesized that machine learning models could accurately make correlations to predict the kinetic rate constant without actually solving the partial differential equations that govern SECM approach curves.

3.1. Multilayer Perceptron Models on Simulated SECM Approach Curves

MLP models are traditionally not conducive for importing two-dimensional data (e.g., current vs time). Thus, we investigated two different feature options. First, we used the raw normalized current value of each point rendering 150 features for each curve. This MLP model trained on these features will be named MLP-C moving forward. The other is selecting the slope of the normalized current and the normalized distance between two consecutive points rendering 149 features for each curve. This MLP model trained on these features will be named MLP-S moving forward.

The MLP-C model consisted of three hidden layers, each of which consisted of 10 nodes (perceptrons). The activation

function for each node in the hidden layer was the rectified linear unit (ReLu). Because this is a regression model, a linear activation function was used for the output layer. The MLP-C model was able to train without showing signs of overfitting. This was confirmed by the decrease of the mean absolute error and the mean-squared error of both the training set and the validation set at a similar rate while training over the 1000 epochs (see Figure S1 for details).

To evaluate the MLP-C model, we fed the model the experimental data from the testing set (i.e., the data that the model did not use for training) and compared the results from the model to the known kinetic rate constants from the analytical equations. As shown in Figure 3, very good agreement between the model prediction and the actual results was obtained. We measured a mean absolute error of 0.14 and a mean-squared error of 0.06 on the testing set. Most of the error is a result of the model's lack of capability to predict extreme rate constant values (e.g., smaller than $10^{-4.5}$ and larger than $10^{-0.5}$). This is because the approach curves at these values are approaching pure negative feedback and pure positive feedback, respectively, and the difference between the approach curves in these regions is very small.

The MLP-S model (the model trained on the normalized slope instead of only the normalized current) consisted of four hidden layers. The first, second, third, and fourth hidden layers consisted of 10, 10, 10, and 5 nodes. Again, the MLP-S model was also able to train without showing signs of overfitting as the mean absolute error and mean-squared error of both the training and validation error decreased at a similar rate (see Figure S2 for details).

Figure 4 shows the model-predicted kinetic rate constant vs the actual kinetic rate constant from the analytical expression. Again very good agreement between the model prediction and the actual results was obtained. In fact, the mean absolute error was measured to be 0.05 and the mean-squared error was measured to be 0.01 for the testing set data. As was the case for the MLP-C model, most of the error in the MLP-S model is a result of the model's lack of capability to predict extreme rate constant values. Note that this model showed improved mean absolute error values and mean-squared error values compared to the model which was trained on the data where the current values were selected as features. This is because slopes contain information regarding the current and tip−substrate distance values. Therefore, we observed that using the slope as a method for incorporating time-dependent experimental data into MLP models can improve their accuracy and predicting power.

3.2. Convolutional Neural Networks

The images used to train the CNN were 3800 grayscale 100 × 100 images of approach curves, each corresponding to a unique substrate rate constant and a final tip−substrate distance pair. The legends and the *x* and *y* axes of the graph were not included. Only the curve alone was included as input, with example images shown in Figure S3.

The CNN was trained as a multiclass classification model, with each approach curve belonging to one of 10 classes. Each class represented a range of rate constant values as shown in Table 1. Just as in the MLP model, each approach curve in the data set had a unique rate constant and final tip/substrate distance combination.

The CNN consisted of two feature extractors, each consisting of two convolutional layers, one max pooling
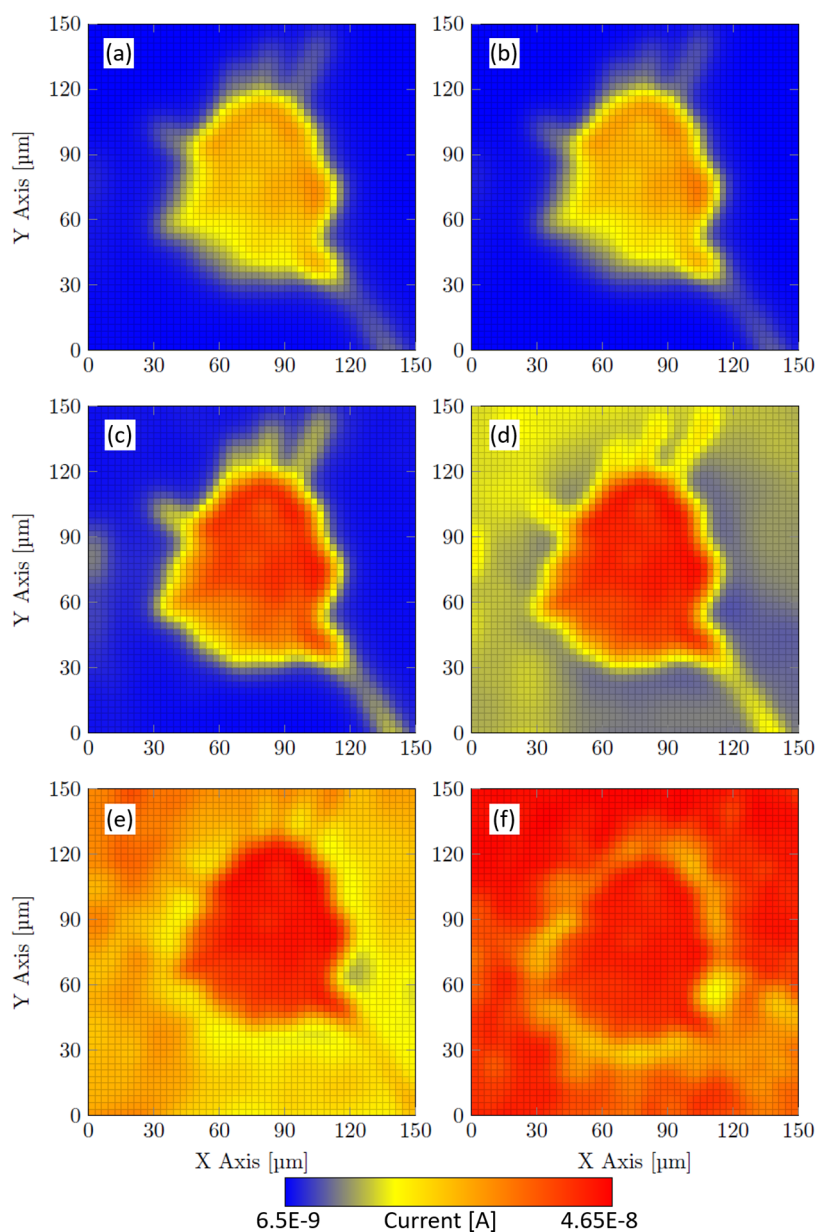
Figure 6. SECM imaging in 10 mM Ru(NH$_3$)$_6$$^{3+}$ with 10 μm Pt tip electrode held at $-$0.3 V vs Ag/AgCl and substrate held at (a) off, (b) +0.05, (c) +0.4, (d) +0.6, (e) +0.7, and (f) +0.8 V vs Ag/AgCl.

layer, with a window size of 2 × 2, and one dropout layer, the rate of which was set to 0.25 to minimize the risk of overfitting by randomly nullifying 25% of the filter parameters. This will reduce complexity, more of which leads to overfitting of the model. In the first convolutional layer, the low-level features of the original image were extracted using a 10 × 10 kernel, outputting a 32 × 32 filter. The most significant features of the filter were extracted using a max pooling layer. The resulting low-level feature map was then sent through the second extractor to extract high-level features using a 5 × 5 kernel, outputting a 64 × 64 filter. A larger filter size was selected for the second extractor to accommodate high-level feature extraction. The most significant features of this filter were then extracted using a final max pooling layer. Finally, the resulting feature map of the convolutional layers was subjected to flattening via a multilayer perception, which consisted of one layer with 256 nodes using the ReLU activation function.

Accuracy, precision, and recall on the testing set were used to evaluate the CNN model, as shown in Table 2. In addition, the confusion matrix showing the accuracy of each of the classes is shown in Figure 5. Examination of Table 2 and Figure 5 shows that the CNN model was able to predict the rate constant to the appropriate class for classes 0−6, which are rate constants ranging from 0.001 to 0.049 cm s^{-1}. Again, this is performed with the model only "looking" at the image without performing any additional calculations. For classes 7− 9, the accuracy is significantly lower; however, the confusion matrix shows that the CNN usually only predicts one class higher or lower than the true class. These inaccurate predictions arise from each of these classes having fast kinetic rate constants with values ranging from 0.05 to 0.1 cm s^{-1}. Thus, each of the approach curves in classes 7−9 have very similar shapes and are approaching a pure positive feedback approach curve (see Figure 2). However, even though the prediction was inaccurate for some curves in these classes,
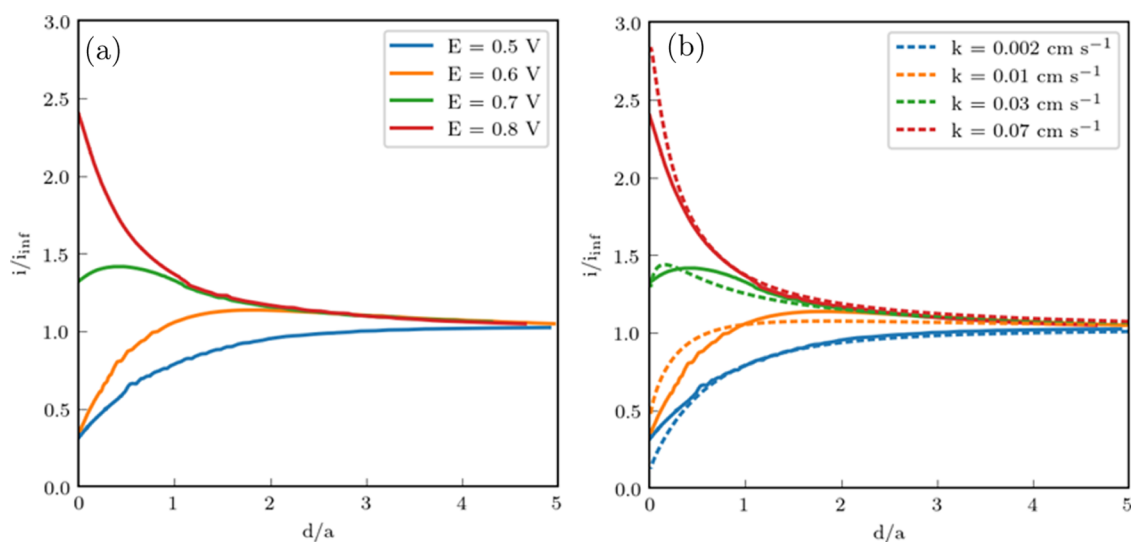
Figure 7. Experimental SECM approach curves of $Ru(NH_3)_6^{3+}$ to $Ru(NH_3)_6^{2+}$ over the Fe-doped nickel (oxy)hydroxide catalyst surface as a function of substrate potential (a). Analytical fits of the experimental approach curve to reveal the kinetics at each potential (b).
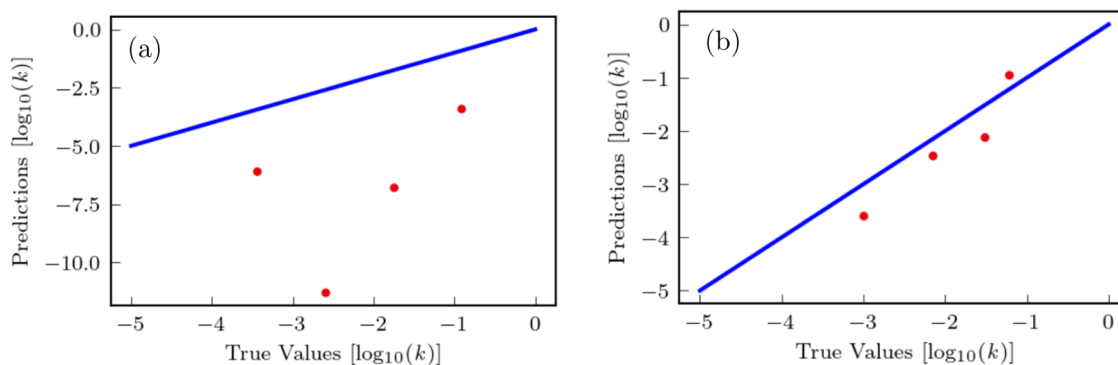

Figure 8. Predicted rate constant vs actual rate constant of the experimental approach curves on the Fe-doped nickel (oxy)hydroxide sample. (a) Predicted vs true values of the MLP-C model and (b) that of the MLP-S model.
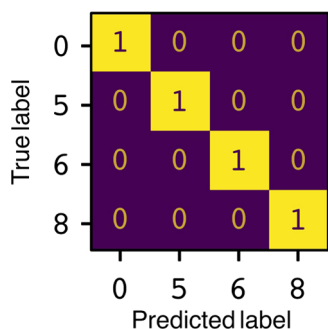

Figure 9. Confusion matrix showing the CNN predicted vs COMSOL determined effective rate constant for the experimental data on the Fe-doped nickel (oxy)hydroxide catalyst sample.

most results were only one class away from the true value. Thus, the model can determine a lower bound for the kinetic rate constant that approaches pure positive feedback and provide a good estimate of the effective rate constant.

3.3. Model Utilization on Experimental Data

As mentioned above, we set out to determine how well these models would work on nonideal experimental approach curves. To do this, we utilized the Fe-doped nickel (oxy)hydroxide as an example material because it is a popular OER catalyst (OER

performance shown in Figure S4) and it holds the unique property of transition from insulating at low positive potentials to conducting at high positive potentials. Thus a single sample can span the entire range of effective kinetic rate constants (i.e., the measured rate encompassing both changes in the conductivity of the electrode and the rate of electron transfer) of outer-sphere, reversible electron-transfer reactions simply by changing the substrate potential.

To demonstrate this, Figure 6a−f shows constant-height SECM images (150 μm × 150 μm) in 10 mM $Ru(NH_3)_6^{3+}$ of the crystalline Fe-doped nickel (oxy)hydroxide electrocatalyst with a defect shown in the center. Here, the Fe-doped nickel (oxy)hydroxide catalyst is on the outside of the defect, and at the defect, the conductive fluorine-doped tin oxide-coated glass is exposed to the electrolyte. For each of these images, the Pt tip electrode is held at −0.3 V vs Ag/AgCl and the substrate is (a) turned off, held at (b) +0.05, (c) +0.4, (d) +0.6, (e) +0.7, and (f) +0.8 V vs Ag/AgCl. While a potential of +0.05 V vs Ag/AgCl should be sufficient to oxidize the $Ru(NH_3)_6^{2+}$ back to $Ru(NH_3)_6^{3+}$ and create positive feedback, this was not shown on the catalyst surface when such potential was applied. This is attributed to significantly slower kinetics on the catalyst surface when in the insulating state. However, the center of the image shows a hole in the catalyst surface, revealing the plain FTO glass in the middle. The FTO region does demonstrate

positive feedback at an applied potential of +0.05 V vs Ag/AgCl. As the substrate potential becomes more positive during the SECM imaging, the positive feedback across the image becomes more prominent. Once the substrate reaches +0.6 V vs Ag/AgCl, the catalyst region transitions from insulating to conducting and is able to turn around the redox species and create a small positive feedback. The FTO glass is at the maximum positive feedback at this potential. Finally, once the substrate reaches +0.8 V vs Ag/AgCl, the catalyst region shows the same maximum feedback as the FTO glass, demonstrating that the electron-transfer step can occur sufficiently fast that the kinetics are no longer the limiting component.

After imaging, the SECM tip approached toward the substrate while holding the substrate at varying potentials. The tip electrode was held constant at −0.3 V vs Ag/AgCl. These experiments resulted in the approach curves shown in Figure 7a. As shown in Figure 7a, the approach curves transition from negative feedback to positive feedback as the potential of the substrate changes from +0.5 to +0.8 V vs Ag/AgCl, verifying the results determined by the SECM imaging. Further, these approach curves were simulated with the analytic expression described in eqs 1−6 assuming a diffusion coefficient of 10^{-5} cm^2 s^{-1}, as shown in Figure 7b. Here, we can see that the rate constant of the substrate varied from 0.001 to 0.07 cm^2 s^{-1}.

To evaluate how well the machine learning models performed on nonideal experimental data, kinetic rate constants for each of the four approach curves shown in Figure 8 were calculated with each of the three models. The performance of the regression MLP models is shown in Figure 8. For the MLP-C model (Figure 8a), the performance is relatively poor compared to the performance on synthetic data. We attribute this poor accuracy to the MLP-C model only using the measured current data, without any z-position data. Thus, nonidealities that may arise from nonflat substrates and imperfect tip/substrate alignment are not captured in the simulated data used to train the model. Thus, the MLP-C model has difficulty capturing the kinetic rate constant of the substrate based on the real approach curve data.

For the MLP-S (Figure 8b) model, there is a significant improvement compared to the performance of the MLP-C model. This improvement is due to the fact that the slope values, which incorporate the z-position data, are a better representation of the approach curves compared to only the measured current values. However, because the MLP-S model relies on the slope, it may be more susceptible to experimental noise in the measured current, which could affect the individual slope calculations.

The results of the CNN model are shown in Figure 9. It is shown that the experimental curves, all of which corresponded to either class 0, 5, 6, or 8 were predicted perfectly. Because CNN models are able to "look" at the approach curves and gauge the direction and the amount of curvature in the approach curve, it acts more like how a human would interpret the data and appears to be less susceptible to nonidealities or experimental noise.

3.4. Conclusions

We have demonstrated that artificial neural networks can be a powerful tool for performing high-throughput data analysis on experimental data. In fact, the CNN used in this study was able to evaluate all 800 approach curves in the testing set in under 400 ms. While analysis via finite element analysis could take over 60 s for a single approach curve. We also identified that feature design is important for the rapid analysis of experimental data. For example, multilayer perceptron models can be used on two-dimensional data if the features can be designed to incorporate both dimensions (e.g., using the slope between the measured current and the z-position for SECM approach curves). A second key finding is that CNN is more apt to handle nonideal data because these models simulate how humans "look" at an image. Thus, CNNs can be very powerful for data that has significant noise or nonidealities and they can provide effective rate constant information on complex electrochemical systems. These advantages outweigh the fact that there is some "blank space" with no information in analyzing images.

Once these artificial neural networks are trained, analyzing the data is extremely rapid and efficient. Thus, we believe that online machine learning will become a powerful tool for high-throughput chemical data analysis.

■ ASSOCIATED CONTENT

Ⓢ Supporting Information

The Supporting Information is available free of charge at https://pubs.acs.org/doi/10.1021/acsmeasureciau.2c00056.

> Training and validation errors for the MLP-C (Figure S1) and MLP-S (Figure S2) model; example images used in the CNN model (Figure S3); additional electrochemical data on the Fe-doped nickel (oxy)-hydroxide electrode (Figure S4); and electrochemical response of the SECM tip electrode (Figure S5) (PDF)

> (PDF)

■ AUTHOR INFORMATION

Corresponding Author

Kevin C. Leonard − *Department of Chemical & Petroleum Engineering, The University of Kansas, Lawrence, Kansas 66045, United States; Center for Environmentally Beneficial Catalysis, The University of Kansas, Lawrence, Kansas 66047, United States;* ● orcid.org/0000-0002-0172-3150; Email: kcleonard@ku.edu

Authors

Dinuka Rajapakse − *Department of Chemical & Petroleum Engineering, The University of Kansas, Lawrence, Kansas 66045, United States; Center for Environmentally Beneficial Catalysis, The University of Kansas, Lawrence, Kansas 66047, United States*

Josh Meckstroth − *Department of Chemical & Petroleum Engineering, The University of Kansas, Lawrence, Kansas 66045, United States*

Dylan T. Jantz − *Department of Chemical & Petroleum Engineering, The University of Kansas, Lawrence, Kansas 66045, United States; Center for Environmentally Beneficial Catalysis, The University of Kansas, Lawrence, Kansas 66047, United States*

Kyle Vincent Camarda − *Department of Chemical & Petroleum Engineering, The University of Kansas, Lawrence, Kansas 66045, United States*

Zijun Yao − *Department of Electrical Engineering & Computer Science, The University of Kansas, Lawrence, Kansas 66045, United States*

Complete contact information is available at:

Author Contributions

CRediT: **Dinuka Rajapakse** data curation (equal), investigation (equal), methodology (equal), software (equal), writing-original draft (equal); **Josh Meckstroth** data curation (equal), formal analysis (equal), investigation (equal), methodology (equal), software (equal); **Dylan T. Jantz** investigation (equal), methodology (equal), writing-review & editing (equal); **Kyle Vincent Camarda** supervision (equal), writing-review & editing (equal); **Zijun Yao** formal analysis (equal), supervision (equal), writing-review & editing (equal); **Kevin C. Leonard** conceptualization (equal), formal analysis (equal), funding acquisition (equal), investigation (equal), methodology (equal), project administration (equal), software (equal), validation (equal), visualization (equal), writing-original draft (equal), writing-review & editing (equal).

Notes

The authors declare no competing financial interest.

◼ REFERENCES

(1) Bard, A. J.; Fan, F.; Kwak, J.; Lev, O. Scanning Electrochemical Microscopy - Introduction and Principles. *Anal. Chem.* **1989**, *61*, 132−138.

(2) Lefrou, C.; Cornut, R. Analytical expressions for quantitative scanning electrochemical microscopy (SECM). *ChemPhysChem* **2010**, *11*, 547−556.

(3) Polcari, D.; Dauphin-Ducharme, P.; Mauzeroll, J. Scanning Electrochemical Microscopy: A Comprehensive Review of Experimental Parameters from 1989 to 2015. *Chem. Rev.* **2016**, *116*, 13234−13278.

(4) Jantz, D. T.; Leonard, K. C. Characterizing Electrocatalysts with Scanning Electrochemical Microscopy. *Ind. Eng. Chem. Res.* **2018**, *57*, 7431−7440.

(5) Bard, A. J.; Mirkin, M.; Unwin, P.; Wipf, D. Scanning Electrochemical Microscopy .12. Theory and Experiment of The Feedback Mode With Finite Heterogeneous Electron-Transfer Kinetics and Arbitrary Substrate Size. *J. Phys. Chem. A* **1992**, *96*, 1861−1868.

(6) Amemiya, S.; Bard, A. J.; Fan, F.-R. F.; Mirkin, M. V.; Unwin, P. R. Scanning Electrochemical Microscopy. *Annu. Rev. Anal. Chem.* **2008**, *1*, 95−131.

(7) Preet, A.; Lin, T.-E. A Review: Scanning Electrochemical Microscopy (SECM) for Visualizing the Real-Time Local Catalytic Activity. *Catalyst* **2021**, *11*, No. 594.

(8) Bard, A. J.; Mirkin, M. V. *Scanning Electrochemical Microscopy*; CRC Press, 2012.

(9) Kai, T.; Zoski, C. G.; Bard, A. J. Scanning electrochemical microscopy at the nanometer level. *Chem. Commun.* **2018**, *54*, 1934−1947.

(10) Bard, A. J.; Fan, F.-R. F.; Pierce, D. T.; Unwin, P. R.; Wipf, D. O.; Zhou, F. Chemical imaging of surfaces with the scanning electrochemical microscope. *Science* **1991**, *254*, 68−74.

(11) Kim, J.; Renault, C.; Nioradze, N.; Arroyo-Currás, N.; Leonard, K. C.; Bard, A. J. Electrocatalytic activity of individual Pt nanoparticles studied by nanoscale scanning electrochemical microscopy. *J. Am. Chem. Soc.* **2016**, *138*, 8560−8568.

(12) Kim, J.; Renault, C.; Nioradze, N.; Arroyo-Currás, N.; Leonard, K. C.; Bard, A. J. Nanometer scale scanning electrochemical microscopy instrumentation. *Anal. Chem.* **2016**, *88*, 10284−10289.

(13) Conzuelo, F.; Schulte, A.; Schuhmann, W. Biological imaging with scanning electrochemical microscopy. *Proc. R. Soc. A* **2018**, *474*, No. 20180409.

(14) Bard, A. J.; Li, X.; Zhan, W. Chemically imaging living cells by scanning electrochemical microscopy. *Biosens. Bioelectron.* **2006**, *22*, 461−472.

(15) Laforge, F. O.; Velmurugan, J.; Wang, Y.; Mirkin, M. V. Nanoscale imaging of surface topography and reactivity with the scanning electrochemical microscope. *Anal. Chem.* **2009**, *81*, 3143−3150.

(16) Jayaraman, S.; Hillier, A. C. Construction and reactivity mapping of a platinum catalyst gradient using the scanning electrochemical microscope. *Langmuir* **2001**, *17*, 7857−7864.

(17) Sun, T.; Zhang, H.; Wang, X.; Liu, J.; Xiao, C.; Nanayakkara, S. U.; Blackburn, J. L.; Mirkin, M. V.; Miller, E. M. Nanoscale mapping of hydrogen evolution on metallic and semiconducting MoS 2 nanosheets. *Nanoscale Horiz.* **2019**, *4*, 619−624.

(18) Sarkar, S.; Wang, X.; Hesari, M.; Chen, P.; Mirkin, M. V. Scanning Electrochemical and Photoelectrochemical Microscopy on Finder Grids: Toward Correlative Multitechnique Imaging of Surfaces. *Anal. Chem.* **2021**, *93*, 5377−5382.

(19) Jantz, D. T.; Balla, R. J.; Huang, S.-H.; Kurapati, N.; Amemiya, S.; Leonard, K. C. Simultaneous Intelligent Imaging of Nanoscale Reactivity and Topography by Scanning Electrochemical Microscopy. *Anal. Chem.* **2021**, *93*, 8906−8914.

(20) Balla, R. J.; Jantz, D. T.; Kurapati, N.; Chen, R.; Leonard, K. C.; Amemiya, S. Nanoscale intelligent imaging based on real-time analysis of approach curve by scanning electrochemical microscopy. *Anal. Chem.* **2019**, *91*, 10227−10235.

(21) Jones, P. J.; Catt, M.; Davies, M. J.; Edwardson, C. L.; Mirkes, E. M.; Khunti, K.; Yates, T.; Rowlands, A. V. Feature selection for unsupervised machine learning of accelerometer data physical activity clusters-A systematic review. *Gait Posture* **2021**, *90*, 120−128.

(22) Hoar, B. B.; Zhang, W.; Xu, S.; Deeba, R.; Costentin, C.; Gu, Q.; Liu, C. Electrochemical mechanistic analysis from cyclic voltammograms based on deep learning. *ACS Meas. Sci. Au* **2022**, DOI: 10.1021/acsmeasuresciau.2c00045.

(23) Kennedy, G. F.; Zhang, J.; Bond, A. M. Automatically identifying electrode reaction mechanisms using deep neural networks. *Anal. Chem.* **2019**, *91*, 12220−12227.

(24) Gundry, L.; Kennedy, G.; Bond, A. M.; Zhang, J. Inclusion of multiple cycling of potential in the deep neural network classification of voltammetric reaction mechanisms. *Faraday Discuss.* **2022**, *233*, 44−57.

(25) Chen, H.; Kätelhön, E.; Le, H.; Compton, R. G. Use of Artificial Intelligence in Electrode Reaction Mechanism Studies: Predicting Voltammograms and Analyzing the Dissociative CE Reaction at a Hemispherical Electrode. *Anal. Chem.* **2021**, *93*, 13360−13372.

(26) Chen, H.; Katelhon, E.; Compton, R. G. Predicting voltammetry using physics-informed neural networks. *J. Phys. Chem. Lett.* **2022**, *13*, 536−543.

(27) Gardner, M. W.; Dorling, S. Artificial neural networks (the multilayer perceptron)—a review of applications in the atmospheric sciences. *Atmos. Environ.* **1998**, *32*, 2627−2636.

(28) Ramchoun, H.; Amine, M.; Idrissi, J.; Ghanou, Y.; Ettaouil, M. Multilayer perceptron: Architecture optimization and training. *Int. J. Interact. Multimedia Artif. Intell.* **2016**, *4*, 26−30.

(29) Murtagh, F. Multilayer perceptrons for classification and regression. *Neurocomputing* **1991**, *2*, 183−197.

(30) Norgaard, M.; Ravn, O.; Poulsen, N. K.; Hansen, L. K. *Neural Networks for Modelling and Control of Dynamic Systems: A Practitioner's Handbook*; Springer, 2000.

(31) Ajit, A.; Acharya, K.; Samanta, A. In *A Review of Convolutional Neural Networks*, 2020 International Conference on Emerging Trends

in Information Technology and Engineering (ic-ETITE), 2020; pp 1−5.

(32) Ilesanmi, A. E.; Ilesanmi, T. O. Methods for image denoising using convolutional neural network: a review. *Complex Intell. Syst.* **2021**, *7*, 2179−2198.

(33) Bernal, J.; Kushibar, K.; Asfaw, D. S.; Valverde, S.; Oliver, A.; Marti, R.; Llado, X. Deep convolutional neural networks for brain image analysis on magnetic resonance imaging: a review. *Artif. Intell. Med.* **2019**, *95*, 64−81.

(34) Anwar, S. M.; Majid, M.; Qayyum, A.; Awais, M.; Alnowami, M.; Khan, M. K. Medical image analysis using convolutional neural networks: a review. *J. Med. Syst.* **2018**, *42*, No. 226.

(35) Schwendicke, F.; Golla, T.; Dreher, M.; Krois, J. Convolutional neural networks for dental image diagnostics: A scoping review. *J. Dent.* **2019**, *91*, No. 103226.

(36) Rawat, W.; Wang, Z. Deep convolutional neural networks for image classification: A comprehensive review. *Neural Comput.* **2017**, *29*, 2352−2449.

(37) Chen, L.; Li, S.; Bai, Q.; Yang, J.; Jiang, S.; Miao, Y. Review of image classification algorithms based on convolutional neural networks. *Remote Sens.* **2021**, *13*, No. 4712.

(38) Al-Saffar, A. A. M.; Tao, H.; Talab, M. A. In *Review of Deep Convolution Neural Network in Image Classification*, 2017 International Conference on Radar, Antenna, Microwave, Electronics, and Tele-communications (ICRAMET), 2017; pp 26−31.

(39) Yang, W.; Jin, L.; Tao, D.; Xie, Z.; Feng, Z. DropSample: A new training method to enhance deep convolutional neural networks for large-scale unconstrained handwritten Chinese character recognition. *Pattern Recognit.* **2016**, *58*, 190−203.

(40) Zhang, S.; Jin, L.; Lin, L. Discovering similar Chinese characters in online handwriting with deep convolutional neural networks. *Int. J. Document Anal. Recognit.* **2016**, *19*, 237−252.

(41) Darmatasia; Fanany, M. I. In *Handwriting Recognition on Form Document Using Convolutional Neural Network and Support Vector Machines (CNN-SVM)*, 2017 5th International Conference on Information and Communication Technology (ICoIC7); IEEE, 2017; pp 1−6.

(42) Maitra, D. S.; Bhattacharya, U.; Parui, S. K. In *CNN Based Common Approach to Handwritten Character Recognition of Multiple Scripts*, 2015 13th International Conference on Document Analysis and Recognition (ICDAR); IEEE, 2015; pp 1021−1025.

(43) Chen, L.; Wang, S.; Fan, W.; Sun, J.; Naoi, S. In *Beyond Human Recognition: A CNN-Based Framework for Handwritten Character Recognition*, 2015 3rd IAPR Asian Conference on Pattern Recognition (ACPR); IEEE, 2015; pp 695−699.

(44) Barforoush, J. M.; Seuferling, T. E.; Jantz, D. T.; Song, K. R.; Leonard, K. C. Insights into the active electrocatalytic areas of layered double hydroxide and amorphous nickel-iron oxide oxygen evolution electrocatalysts. *ACS Appl. Energy Mater.* **2018**, *1*, 1415−1423.

(45) Barforoush, J. M.; Jantz, D. T.; Seuferling, T. E.; Song, K. R.; Cummings, L. C.; Leonard, K. C. Microwave-assisted synthesis of a nanoamorphous (Ni 0.8, Fe 0.2) oxide oxygen-evolving electrocatalyst containing only "fast" sites. *J. Mater. Chem. A* **2017**, *5*, 11661−11670.

(46) Seuferling, T. E.; Larson, T. R.; Barforoush, J. M.; Leonard, K. C. Carbonate-Derived Multi-Metal Catalysts for Electrochemical Water-Splitting at High Current Densities. *ACS Sustainable Chem. Eng.* **2021**, *9*, 16678−16686.

(47) Barforoush, J. M.; McDonald, T. D.; Desai, T. A.; Widrig, D.; Bayer, C.; Brown, M. K.; Cummings, L. C.; Leonard, K. C. Intelligent scanning electrochemical microscopy tip and substrate control utilizing fuzzy logic. *Electrochim. Acta* **2016**, *190*, 713−719.